Supplementary Information for

Direct Resolution of Three-Dimensional Gaze for Spatial Interaction via a Smart Contact Lens

Xinyuan Jia[1,2], Binchen Zhao[3], Jiaju Yin[1,2], Haorong Li[4], Jiong Pan[1,2], Zigan Xu[1,2], Zeda Wang[1,2], Lu-Qi Tao[2,*], Yi Yang[1,2,*] and Tian-Ling Ren[1,2,*].

[1]School of Integrated Circuits, Tsinghua University, Beijing 100084, China.
[2]Beijing National Research Center for Information Science and Technology (BNRist), Tsinghua University, Beijing 100084, China.
[3]School of Integrated Circuits, Peking University, Beijing 100871, China.
[4]Weiyang College, Tsinghua University, Beijing 100084, China.
* Corresponding author. RenTL@tsinghua.edu.cn, yiyang@tsinghua.edu.cn, taoluqi@tsinghua.edu.cn

Table of contents

Supplementary Note: Theoretical basis for multi-coil readout, directional discriminability, and channel decoupling.
To support the design logic of the proposed multi-coil RLC lens, we summarize here the reader-side impedance model, the physical basis for directional discriminability, and the approximate decoupling between curvature-dependent frequency shifts and direction-dependent amplitude variations.

1. Reader-side model of the inductively coupled resonant system

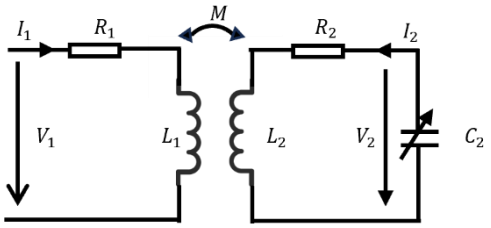

Fig Note2

The wireless readout can be described using the standard equivalent circuit of an inductively coupled primary–secondary resonant system, where the reader coil acts as the primary coil and each lens-integrated resonator acts as a secondary coil. For a single resonant channel, the primary-side voltage and current satisfy[1]:

$$V_1 = R_1 I_1 + sL_1 I_1 + sMI_2 \tag{1}$$

$$V_2 = R_2 I_2 + sL_2 I_2 + sMI_1 \tag{2}$$

Where V_1, V_2 and I_1, I_2 represent the voltage and current on the primary side and secondary side of the inductive coils, respectively. R_1 and R_2 denote the equivalent series resistance of the primary and secondary sides of the inductive coils, respectively. The complex frequency is denoted by $s = j\omega = j2\pi f$

The mutual inductance is given by

$$M = k\sqrt{L_1 L_2} \tag{3}$$

where k is the coupling coefficient.

The intrinsic resonance frequency f_s and quality factor Q of the resonant channel are

$$f_s = \frac{1}{2\pi\sqrt{L_2 C_2}} \tag{4}$$

$$Q = \frac{1}{R_2}\sqrt{\frac{L_2}{C_2}} \tag{5}$$

By combining Eqs. (1)–(5), the equivalent impedance seen at the reader can be written in the standard form:

$$Z_1 = \frac{V_1}{I_1} = R_1 + j2\pi f L_1 + \frac{(2\pi f)^2 M^2}{R_2 + j\left(2\pi f L_2 - \frac{1}{2\pi f C_2}\right)} \tag{6}$$

Its real part is

$$Re\{Z_1\} = R_1 + 2\pi f L_1 k^2 Q \frac{\frac{f}{f_s}}{1 + Q^2(\frac{f}{f_s} - \frac{f_s}{f})^2} \tag{7}$$

Equation (7) shows that the measured spectrum is jointly determined by the resonance parameters (f_s, Q) and the coupling coefficient k. In the present system, curvature-induced deformation primarily perturbs the resonant parameters by changing the effective coil geometry, whereas eye rotation and relative misalignment primarily modulate the coupling coefficient between the lens coil and the reader. This distinction forms the basis for the dual-channel readout strategy.

2. Directional discriminability enabled by the asymmetric three-coil layout

Directional sensing is not inferred from a single resonant channel, but from the joint response of three geometrically non-equivalent coils. Let the eye-rotation state within the operating range be parameterized by (x, y), representing the horizontal and vertical components of gaze rotation. For each resonant channel, an amplitude-based feature A_i can be extracted from the spectrum, such as the resonance-peak magnitude or the linear S_{11} value. The three-coil response can therefore be written as

$$A(x,y) = \begin{bmatrix} A_1(x,y) \\ A_2(x,y) \\ A_3(x,y) \end{bmatrix} \tag{8}$$

If the three coils were identical and arranged with mirror or rotational symmetry, opposite or mirrored eye rotations could in principle generate indistinguishable perturbation patterns, resulting in directional ambiguity. In the present design, coils 1 and 2 preserve similar spiral layouts to maintain comparable common-mode sensitivity to curvature-dependent deformation, while coil 3 intentionally adopts a distinct geometry and orientation to break this symmetry. As a result, eye-rotation–induced asymmetric deformation is projected onto three non-equivalent resonant channels.

Under small rotational perturbations, the channel responses can be linearized as

$$\Delta A_i \approx s_{ix}\Delta x + s_{iy}\Delta y \tag{9}$$

or equivalently,

$$\begin{bmatrix} \Delta A_1 \\ \Delta A_2 \\ \Delta A_3 \end{bmatrix} \approx \begin{bmatrix} s_{1x} & s_{1y} \\ s_{2x} & s_{2y} \\ s_{3x} & s_{3y} \end{bmatrix} \begin{bmatrix} \Delta x \\ \Delta y \end{bmatrix} \tag{10}$$

Here, s_{ix} and s_{iy} denote the directional sensitivities of the i-th channel to horizontal and vertical eye rotation, respectively. If these sensitivity vectors were identical or mutually collinear, the three-coil readout would degenerate into a low-selectivity response. By contrast, the asymmetric geometry of coil 3 makes its directional sensitivity differ from those of coils 1 and 2, thereby suppressing symmetry-induced degeneracy and producing distinguishable multi-channel response patterns over the physiological operating range. Accordingly, the subsequent decoding algorithm is built on a physically structured encoding mechanism rather than on arbitrary empirical correlation.

3. Approximate decoupling of resonance frequency and amplitude-based readout

The decoupling of curvature and direction arises because these two perturbations affect different dominant parameters of the inductive system. Curvature-induced deformation primarily changes the effective inductance of the resonant coil. Since

$$f_s = \frac{1}{2\pi\sqrt{LC}} \tag{11}$$

a small perturbation gives

$$\frac{\Delta f_s}{f_s} \approx -\frac{1}{2}\frac{\Delta L}{L} - \frac{1}{2}\frac{\Delta C}{C} \tag{12}$$

In the present device, the dominant contribution is attributed to deformation-induced geometric changes of the spiral coil, such that the frequency shift mainly reflects curvature variation. By contrast, eye rotation and lateral displacement mainly alter the relative position and orientation between the lens coil and the reader, and therefore perturb the coupling coefficient k.

From Eq. (7), for sufficiently high Q, the resonance feature becomes sharper and the frequency corresponding to the maximum of $Re\{Z_1\}$ approaches the intrinsic resonant frequency[1].

$$f_{peak} \approx f_s \tag{13}$$

At the same time, the resonance amplitude scales strongly with coupling strength and quality factor,

$$A_{peak} \propto k^2 Q \tag{14}$$

indicating that amplitude-based features are much more sensitive to coupling variation than to small intrinsic frequency shifts. Therefore, to first order,

Δf_{peak} is dominated by Δf_s, ΔA_{peak} is dominated by Δk.

This provides the theoretical basis for using resonance frequency as the primary readout of curvature-related deformation and amplitude-based features, including linear S_{11}, as the more sensitive indicators of direction-dependent coupling variation.

This approximation holds when reader-side parasitic capacitance is negligible or sufficiently stable to be absorbed into calibration. Previous analyses of wireless RLC resonant systems have shown that non-negligible parasitic capacitance may reintroduce coupling dependence into the apparent resonance position. Within the operating regime used here, however, the simulated and experimental results are consistent with the above first-order decoupling picture.

Reference	Year	Measurement method	Accommodation control	Reported corneal curvature change	Key interpretation
[2]	2001	Modified keratometer (central)	Convergence controlled	**~0.3–0.5 D** (≥1 meridian, subject-dependent)	Early evidence of measurable corneal shape change with accommodation
[3]	2001	Modified keratometer	Convergence controlled	**0.25–0.6 D**	Independent confirmation under controlled conditions
[4]	2003	Placido corneal topography	Partial (near vs far)	**~0.1–0.3 D** central steepening	Small but systematic curvature change during accommodation
[5]	2005	Corneal topography + ciliary contraction	Partial	**~0.1 D**	Interpreted as secondary mechanical effect of accommodation
[6]	2003	High-resolution videokeratography	Near (0.2 m) vs far (4.0 m)	Radius change **~0.26 mm** (**~0.16 D**); shape change **~1–2 µm**	Statistically significant, spatially resolved corneal shape change
[7]	**2019**	**Dual-Scheimpflug + Placido tomography (GALILEI G2)**	Near (0.25 m) vs far (6 m)	**All participants showed statistically significant changes; mean ±0.1 D regionally**	Large-sample modern study confirming ubiquitous but sub-clinical accommodative corneal changes

Supplementary Table.1: Physiological basis of corneal curvature changes during accommodation

Table S1 summarizes representative studies that have examined corneal shape or curvature changes associated with ocular accommodation under controlled or partially controlled conditions. Despite differences in measurement modality, subject population, and experimental paradigm, these studies consistently report small but repeatable accommodative corneal changes, typically on the order of ~0.1–0.5 diopters. When expressed in terms of corneal curvature radius, the reported changes correspond to variations on the order of tens to a few hundred micrometers at the anterior corneal surface, resulting in relative curvature changes that are readily resolvable by sensitive curvature-sensing modalities.

Across multiple independent studies, accommodative corneal changes exhibit consistent qualitative trends—most commonly a modest increase in anterior corneal curvature under near viewing—despite substantial inter-individual variability and methodological differences. Many prior investigations assessed accommodation using discrete near–far viewing conditions, reflecting the experimental scope of conventional ophthalmic imaging. These measurements therefore represent endpoint observations of a continuous physiological process, and differences in reported significance across studies primarily arise from variations in measurement sensitivity and experimental configuration rather than fundamental physiological inconsistency.

Collectively, these findings establish accommodative corneal curvature change as a stable and reproducible physiological phenomenon. This motivates the approach adopted in the present work: rather than resolving corneal deformation through optical imaging, we directly sense curvature-related changes via resonant frequency shifts in a contact-lens–based platform, enabling reliable estimation of fixation distance from a physiological signal that has been repeatedly observed across diverse measurement paradigms.

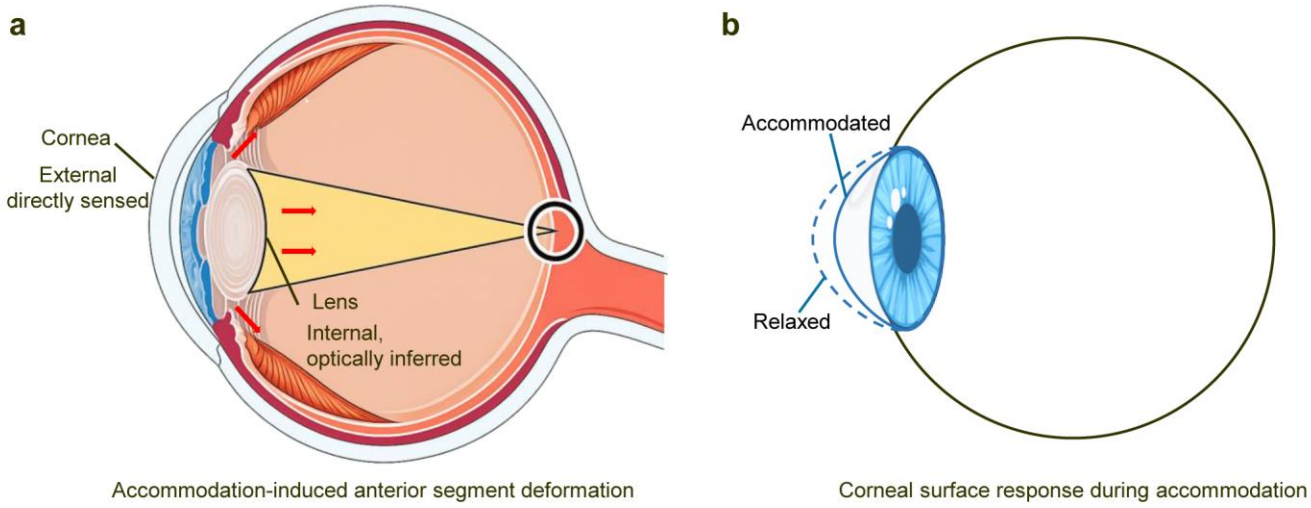

Supplementary Fig. 1: Rationale for using corneal curvature as an embodied depth proxy.

Accommodation involves coordinated physiological responses across multiple ocular structures, including the crystalline lens, ciliary muscle, and anterior segment tissues. Accordingly, multiple internal optical and biomechanical states change during accommodative effort. The present work does not aim to isolate or model all accommodative components; instead, it identifies corneal curvature as a practical and reliable proxy for fixation depth based on accessibility, mechanical inevitability, and sensing robustness.

First, the cornea constitutes the front-end structure of the ocular optical system and is the only accommodation-related component that is both externally exposed and mechanically constrained by surrounding tissue. In contrast to internal structures such as the crystalline lens, whose state must be inferred indirectly through optical imaging or wavefront reconstruction, corneal geometry can be directly sensed without access to the intraocular space. This distinction is particularly relevant for wearable and contact-lens–based platforms, where non-invasive and line-of-sight–independent sensing is required.

Second, relative to the crystalline lens, corneal curvature exhibits reduced hysteresis and does not rely on active shape actuation. While lens deformation arises from complex elastic and viscoelastic responses of internal tissue, corneal curvature changes primarily reflect passive mechanical coupling within the anterior segment during accommodation. Here, hysteresis is discussed at a qualitative engineering level rather than as a detailed biomechanical characterization of ocular tissue. As a result, corneal curvature provides a stable and repeatable geometric signal for sensing purposes, even though it is not the primary contributor to refractive power adjustment.

Third, changes in corneal curvature represent a necessary mechanical consequence of accommodation. Contraction of the ciliary muscle and associated anterior segment deformation inevitably lead to subtle but measurable changes in corneal surface geometry. Consistent with prior studies summarized in Table S1, these changes are reproducible across subjects and measurement modalities. Importantly, their presence does not depend on any specific optical model or imaging technique, underscoring their physiological inevitability rather than a methodological artifact.

Taken together, these considerations motivate the use of corneal curvature as an embodied depth proxy. Rather than claiming uniqueness or dominance among accommodative signals, the present work leverages the fact that corneal curvature changes are externally accessible, mechanically unavoidable, and sufficiently stable to be sensed reliably. This enables fixation distance estimation in three-dimensional gaze interaction without reliance on binocular geometry or internal optical reconstruction, aligning physiological inevitability with engineering practicality.

Supplementary Fig. 2: Geometric design and layout of the asymmetric spiral inductors.
Layout of the three planar spiral inductors integrated on the contact-lens platform. Coils 1 and 2 share identical spiral geometries, with coil 2 uniformly scaled to ~0.8× of coil 1, resulting in two well-separated resonance frequencies while maintaining similar deformation sensitivity for common-mode curvature sensing. Coil 3 adopts a distinct spiral geometry and orientation due to area constraints, providing enhanced sensitivity to asymmetric deformation associated with eye rotation and enabling improved gaze-direction discrimination. Detailed geometric parameters are summarized in Supplementary Table X.

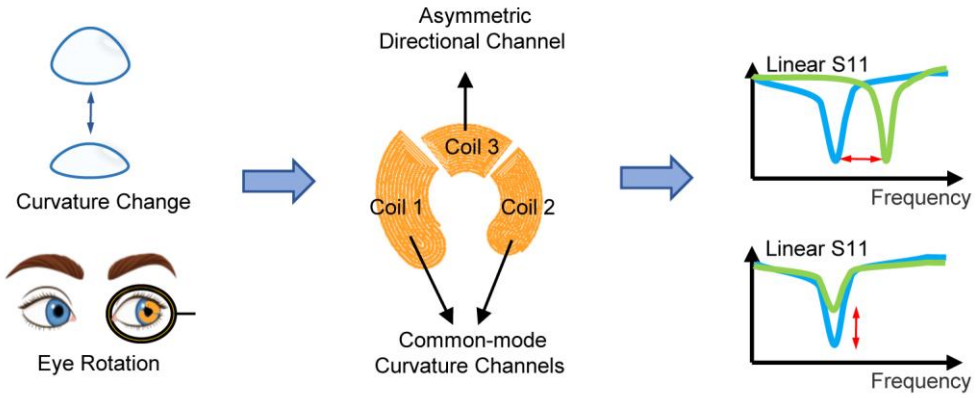

Supplementary Fig. 3: Principle of curvature and direction sensing using multi-coil RLC resonance.
Schematic illustration of the sensing principle underlying the proposed inductive RLC platform. Curvature-induced deformation of the contact-lens substrate leads to small geometry changes in embedded planar spiral coils, resulting in corresponding shifts in their effective inductance and resonance frequency. Following established models of spiral-inductor–based curvature sensors, these frequency shifts provide a measurable proxy for surface curvature.
In the present system, coils 1 and 2 share the same geometry at different scales, enabling curvature estimation through their common-mode resonance-frequency response, which is insensitive to gaze direction. In contrast, coil 3 adopts a distinct layout and orientation, yielding differential spectral responses under asymmetric deformation associated with eye rotation. This separation of common-mode (curvature) and differential (directional) components enables decoupled estimation of fixation distance and gaze direction at the signal level.

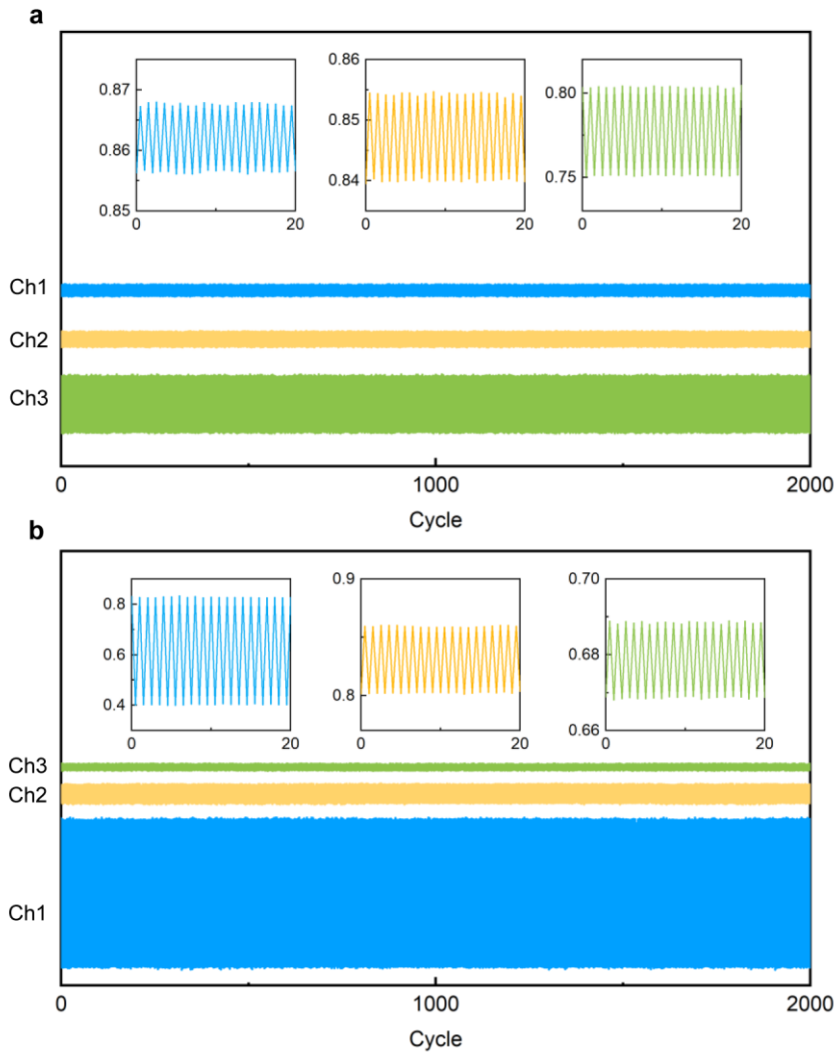

Supplementary Fig. 4: **Cyclic repeatability of Linear S11 under yaw and pitch rotation.**
Cyclic responses of the smart contact lens during repeated rotational motion (±10° yaw and ±20° pitch). Linear S11 signals remain stable over 2000 cycles without observable degradation.

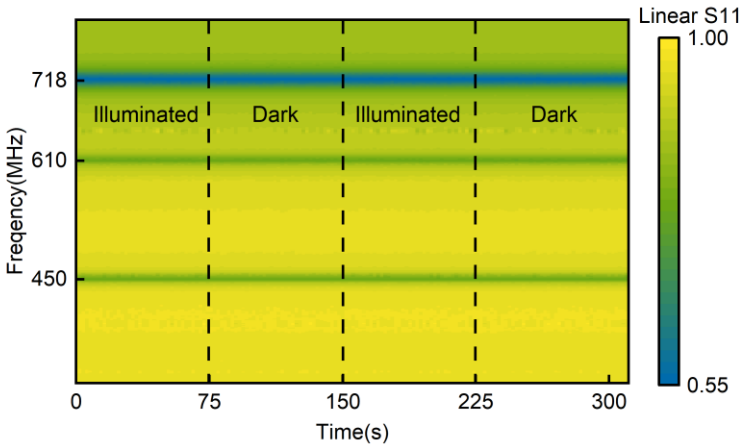

Supplementary Fig. 5: **Effect of ambient lighting conditions on resonance characteristics.**
Resonance frequencies and reflection amplitudes (Linear S11) remain unchanged under illuminated and dark conditions, indicating that both curvature-based depth sensing and directional tracking are insensitive to ambient illumination.

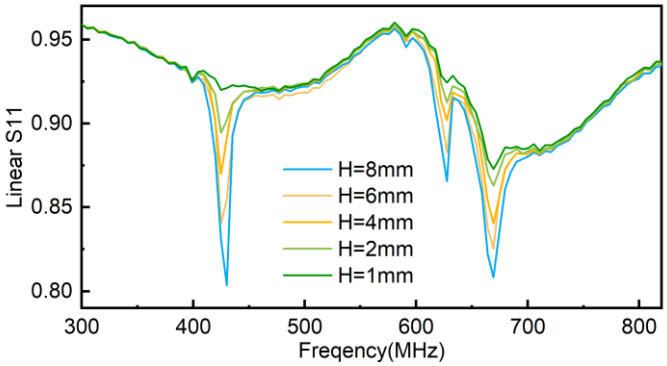

Supplementary Fig. 6: **Influence of reader–lens distance on resonance spectra.**

Linear S11 spectra measured at different distances between the reader coil and the smart contact lens. Variations in coil position primarily induce common-mode changes in resonance amplitude, while resonance frequencies remain stable. The end-side algorithm (Fig. 6) compensates for such amplitude perturbations, enabling robust directional and curvature decoding under distance fluctuation.

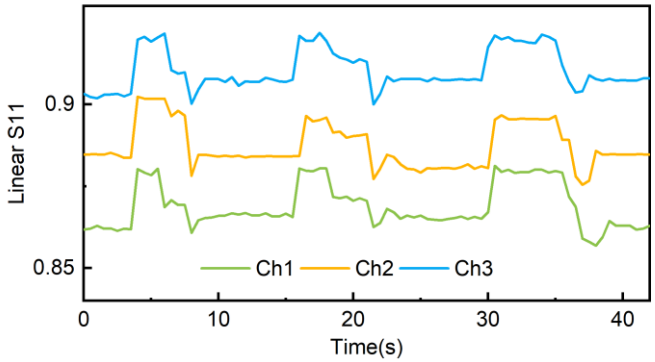

Supplementary Fig. 7: Linear S11 variation during blinking at different speeds.

Linear S11 responses during blinking at different speeds, showing common-mode modulation across channels, consistent with eyelid-induced electromagnetic absorption and distinguishable from directional eye-movement signals.

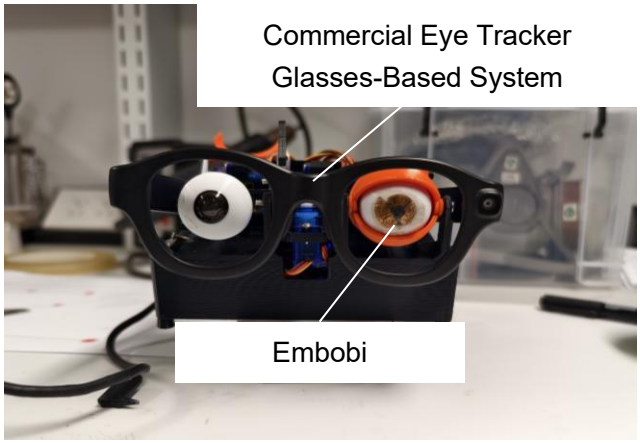

Supplementary Fig. 8: **Mechanical-eye platform for comparison between Embobi and a commercial eye tracker.**

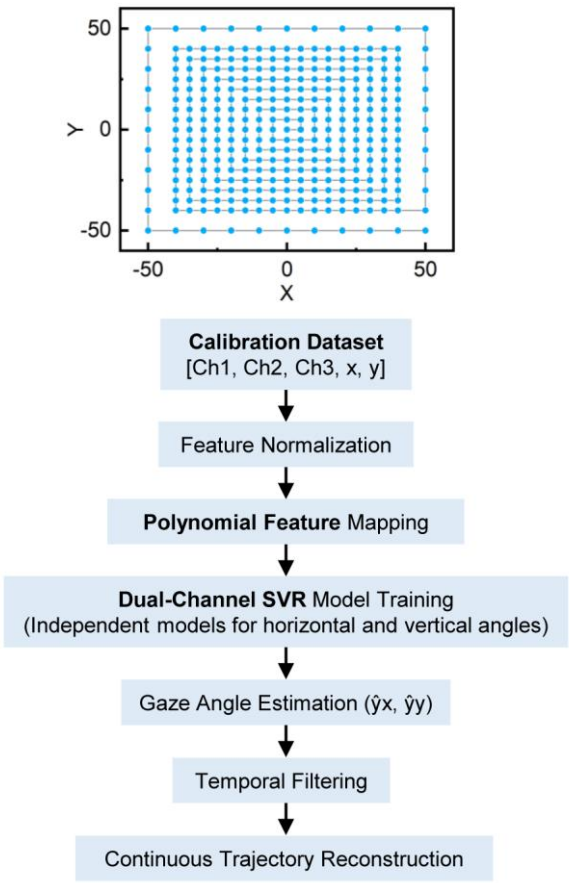

Supplementary Fig. 9: Gaze-direction decoding model.

Gaze-direction estimation was implemented using a supervised regression framework. During calibration, resonance-peak amplitudes from three channels (Ch1–Ch3) were recorded together with ground-truth gaze coordinates (x, y). These data were used to construct a mapping model between spectral features and gaze angles.

All input features were first standardized using a scaler fitted exclusively on calibration data to ensure consistent normalization during inference. Polynomial feature expansion (degree 2–5) was applied to capture nonlinear coupling among resonance channels.

Two independent support vector regression (SVR) models with radial basis function (RBF) kernels were trained to estimate horizontal (x) and vertical (y) gaze components separately. Hyperparameters (polynomial degree, C, and gamma) were optimized via grid search using validation error (RMSE) as the selection criterion.

During inference, incoming spectral amplitudes were transformed using the pretrained scaler and polynomial mapping before being passed to the trained SVR models. To suppress high-frequency jitter, Gaussian smoothing was optionally applied to the predicted gaze trajectory. Predicted coordinates were bounded within the predefined angular range.

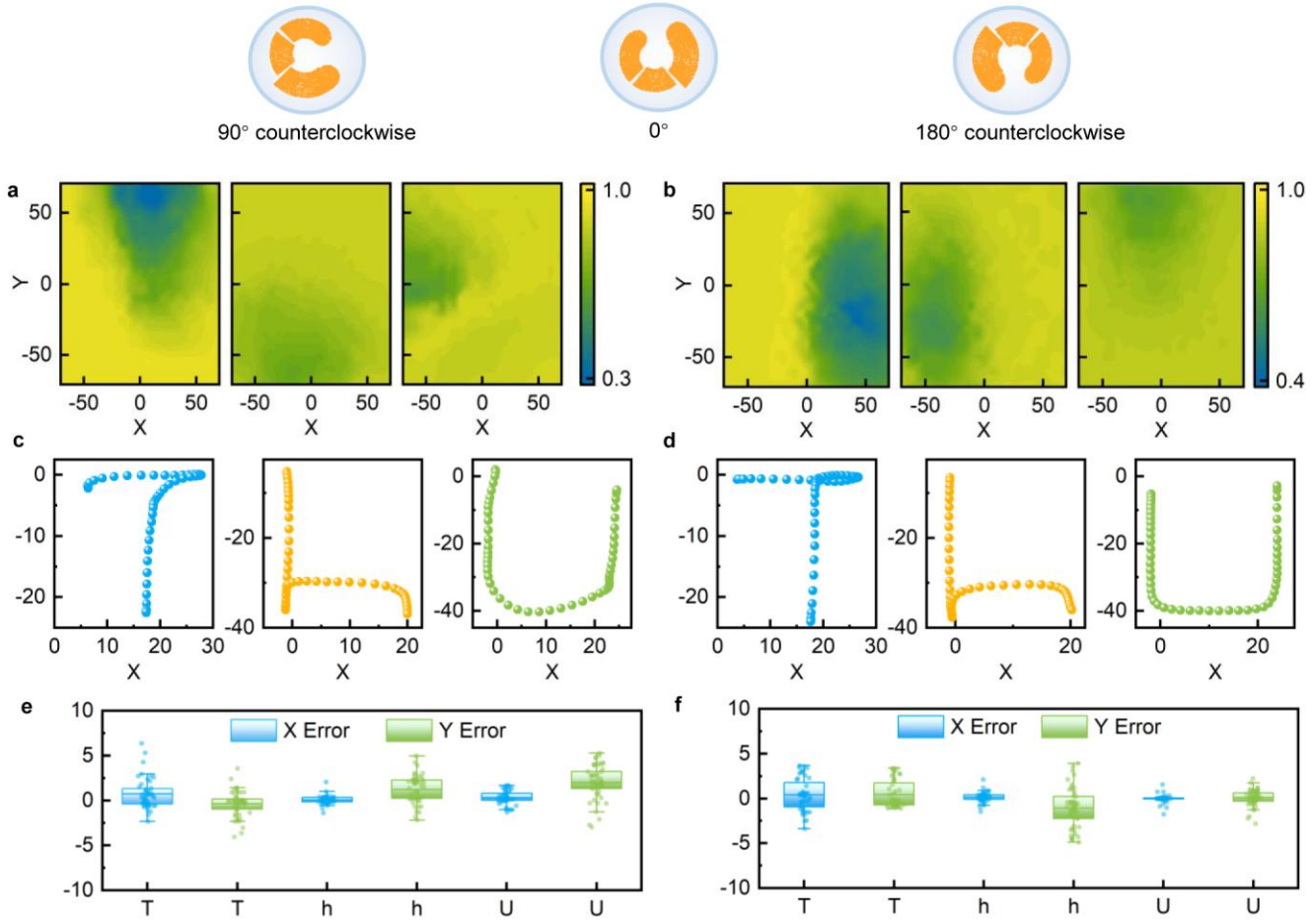

Supplementary Fig. 10: **Influence of lens rotational orientation on directional tracking performance.**
(a,b) Calibration S11 heat maps under 90° and 180° counterclockwise lens rotations. **(c,d)** Reconstructed "ThU" trajectories under corresponding rotation conditions. **(e,f)** X/Y tracking error distributions.
Directional accuracy remains comparable to commercial eye trackers, indicating rotation-invariant decoding; resonance frequencies remain stable under lens rotation.

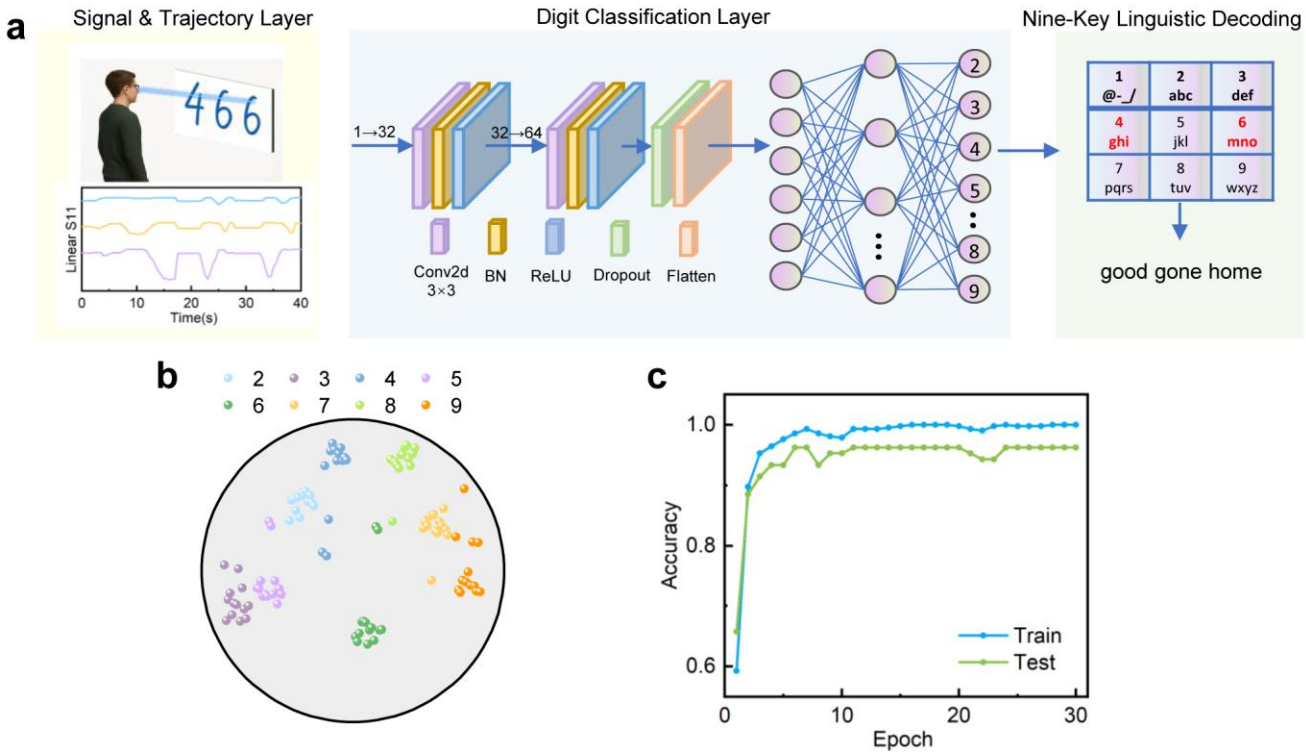

Supplementary Fig. 11: **Trajectory-encoded nine-key input enabled by embodied 3D gaze.**
(a) Architecture for continuous trajectory-to-digit decoding and nine-key linguistic mapping, beyond dwell-based point selection. **(b)** Low-dimensional feature distribution of digit trajectories. **c**, Training and test accuracy of lightweight digit classifier

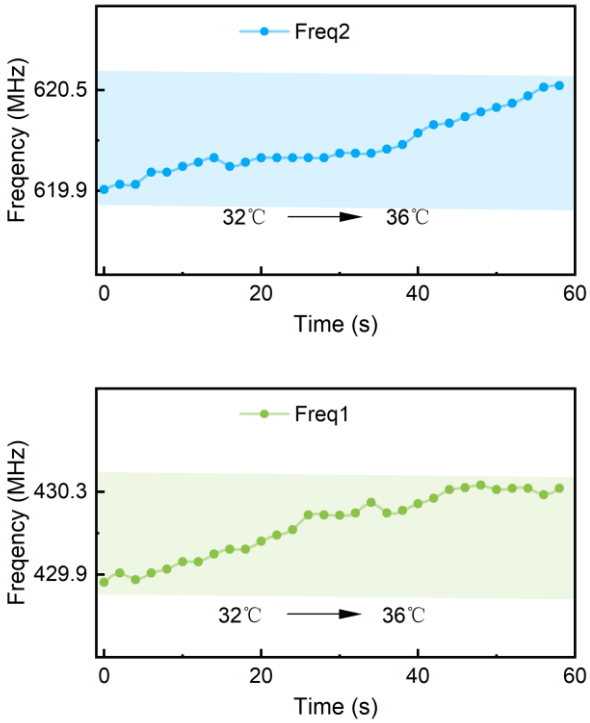

Supplementary Fig. 12: **Influence of ocular-surface temperature variation on resonant frequency.**

Measured resonance-frequency responses of the two sensing coils (Freq1 and Freq2) as temperature was varied from 32 °C to 36 °C, covering the physiological range of human ocular surface temperature[8–10]. Within this interval, both resonators show only minor frequency drift compared with the multi-megahertz resonance shifts associated with accommodation-induced corneal curvature changes described in the main text. This limited temperature sensitivity indicates that physiological thermal fluctuations introduce only small perturbations to the sensing signal. In practical implementations, such residual drift can be further reduced through calibration or algorithmic temperature compensation[11].

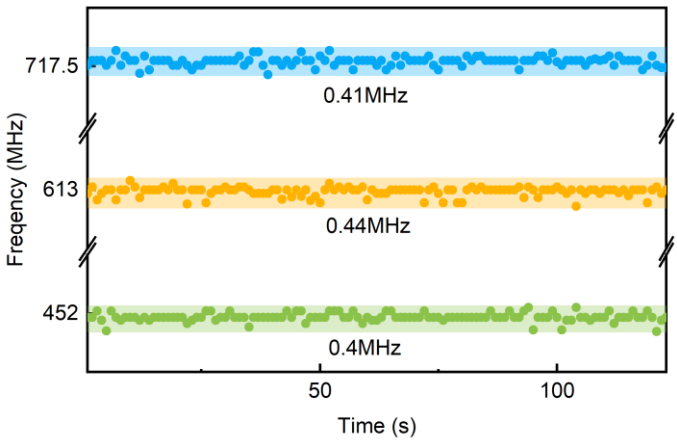

Supplementary Fig. 13: Resonance stability during calibrated eye-rotation without curvature change.
Resonant-frequency traces of the three coils during calibrated rotational motion of the mechanical eye without induced curvature change. The peak-to-peak fluctuation remains below 0.5 MHz (relative shift < 10^{-3}), indicating that directional motion introduces only minor perturbation compared with curvature-induced modulation.

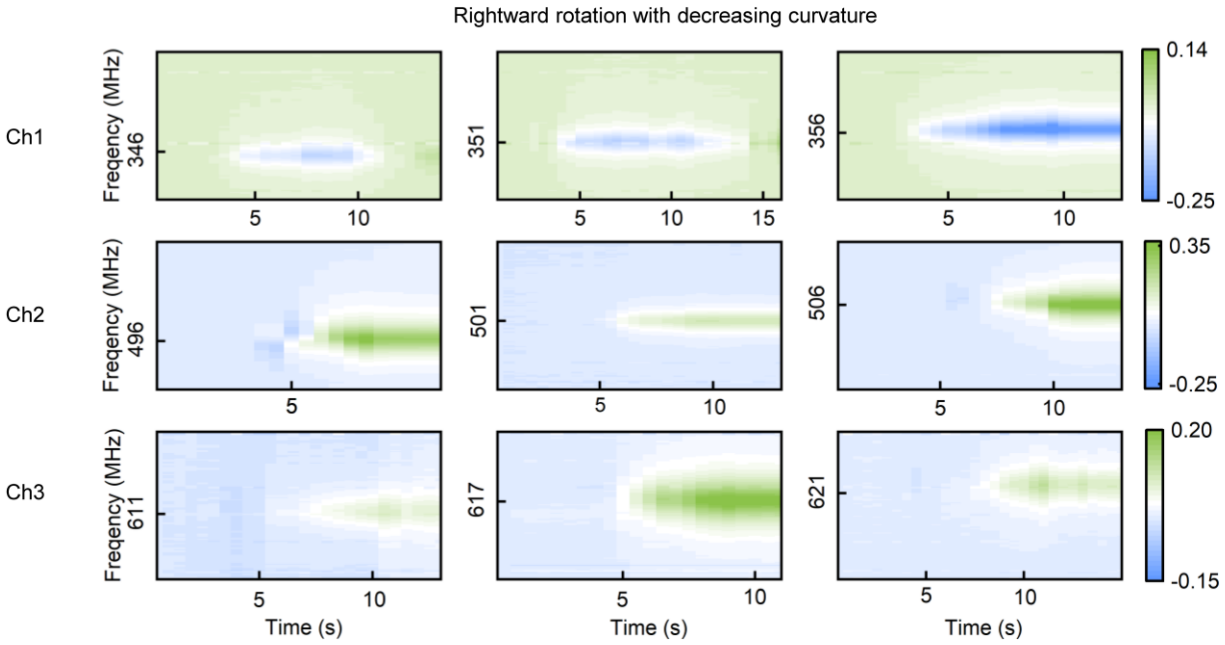

Supplementary Fig. 14: Spectral response of the three resonance channels during rightward eye rotation at different curvature states.

Spectral maps (ΔS11) of the three resonance channels during controlled rightward rotation of the biomimetic eye at multiple corneal-curvature states. Across curvature conditions, the resonance frequencies remain stable during rotation, while the channel responses exhibit a consistent directional signature (Ch1 decreases; Ch2 and Ch3 increase), indicating curvature-invariant directional encoding and effective decoupling between rotation and curvature sensing.

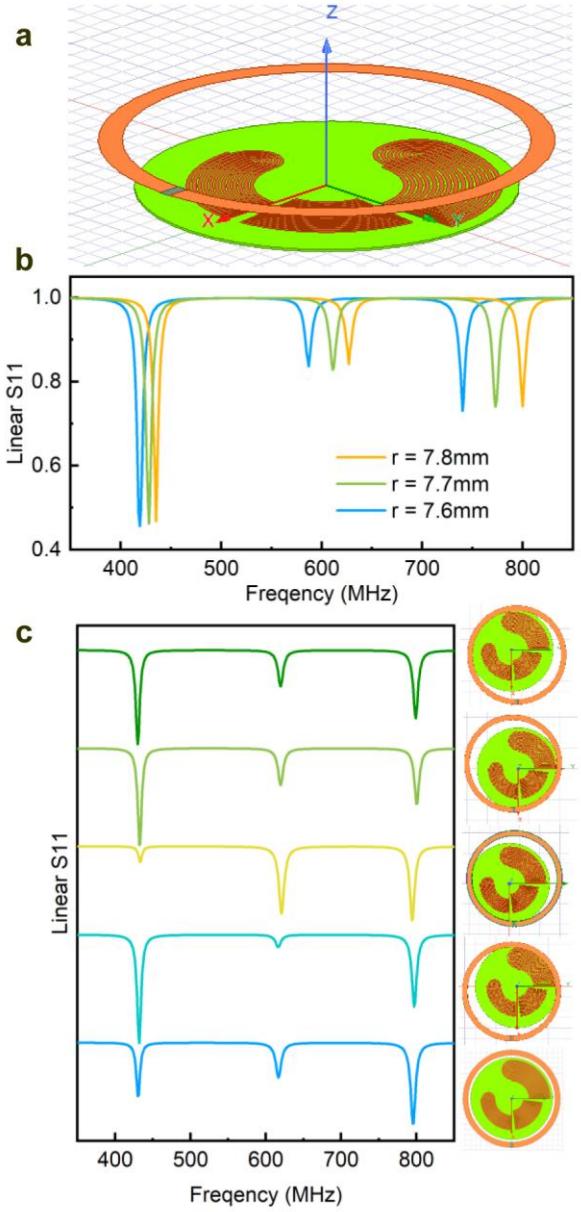

Supplementary Fig. 15: HFSS simulation of channel decoupling between resonance frequency and linear S11.
(a) Three-dimensional electromagnetic model of the device used for simulation.
(b) Simulated linear S11 spectra for devices with different curvature radii (r = 7.6, 7.7, and 7.8 mm).
(c) Simulated linear S11 spectra when the device is laterally displaced relative to the reading coil in four directions, with the corresponding positional configurations shown on the right.

Electromagnetic simulations were performed in HFSS to evaluate the feasibility of decoupling resonance frequency and linear S11 as two independent sensing channels. Supplementary Fig. Xa shows the three-dimensional device model used in simulation. For curvature radii ranging from 7.6 to 7.8 mm, which are close to the physiological anterior corneal radius, the resonance dips underwent pronounced frequency shifts, whereas the associated changes in linear S11 magnitude were comparatively small (Supplementary Fig. 15b). This result indicates that resonance frequency is substantially more sensitive to curvature variation within this physiologically relevant range. In contrast, when the device was displaced laterally relative to the reading coil along four directions, the linear S11 response varied more strongly, while the resonance frequency remained comparatively stable (Supplementary Fig. 15c), indicating that linear S11 is more sensitive to positional misalignment. The simulated trend of frequency variation agrees well with the experimental results in the main text, supporting the proposed functional decoupling of deformation-related and position-related sensing modalities.

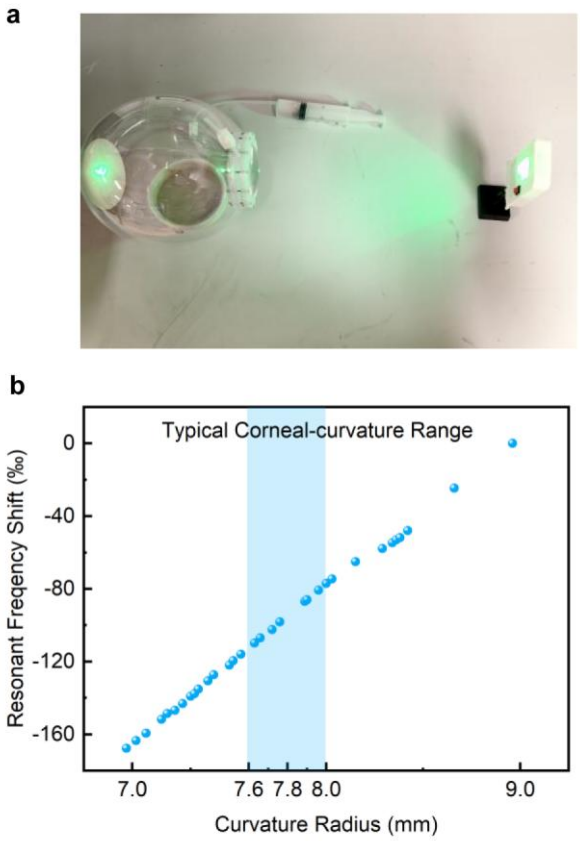

Supplementary Fig. 16: Optical-model illustration and device response range for corneal-curvature variation.
(a) Water-lens optical model used to illustrate depth-dependent focusing behavior. **(b)** Resonant frequency shift as a function of corneal-curvature radius, showing the operating detection range of the device; the shaded region indicates a typical corneal-curvature range. Near/Mid/Far depth levels in interaction are defined by subject-specific relative curvature changes rather than fixed absolute curvature-radius thresholds.

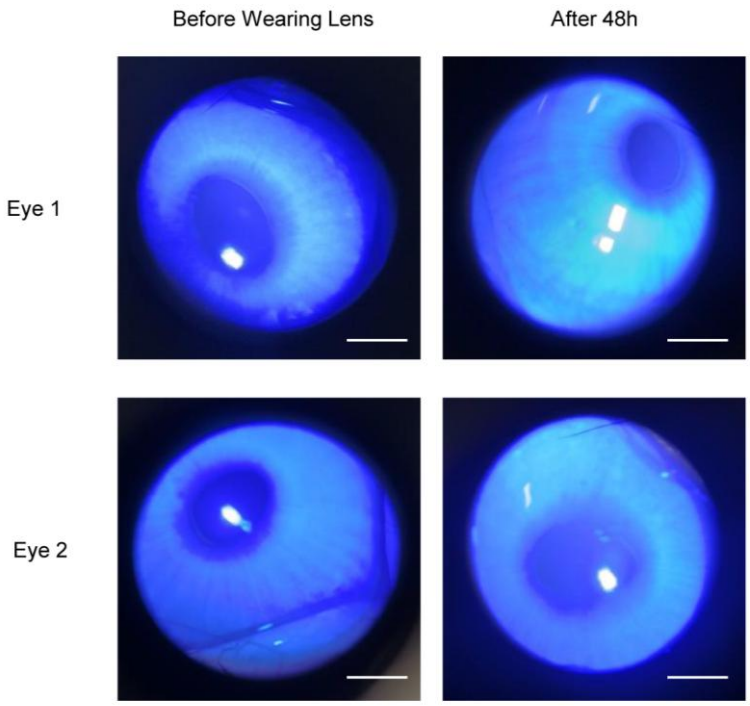

Supplementary Fig. 17: **Slit lamp photographs of two rabbit eyes before and after 48 hours of Embobi wear. Scale bar, 5 mm.** The corneal surface shows no significant damage after 48 hours of Embobi wear, demonstrating the safety of Embobi.

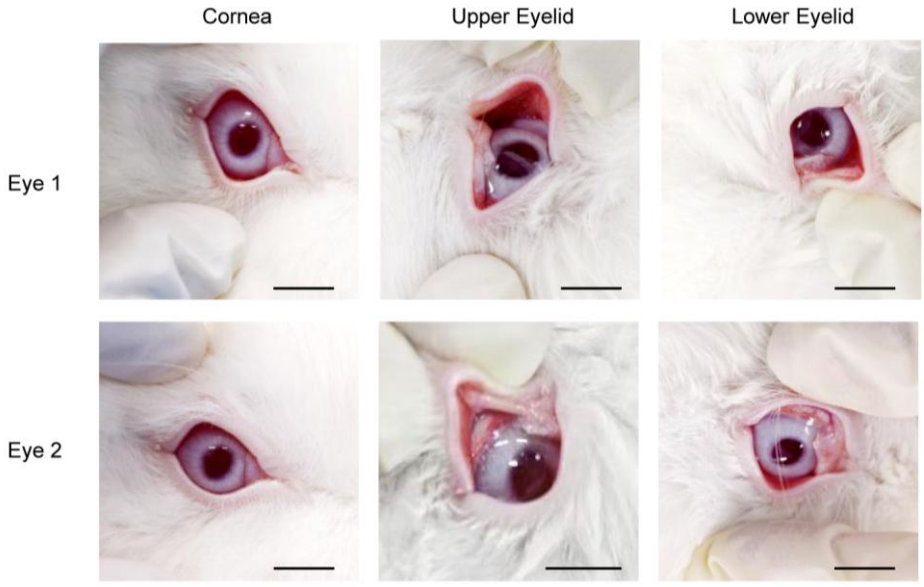

Supplementary Fig. 18: Photographs of the cornea and upper and lower eyelids after 48 h of Embobi wear in rabbits. Scale bar, 1 cm.

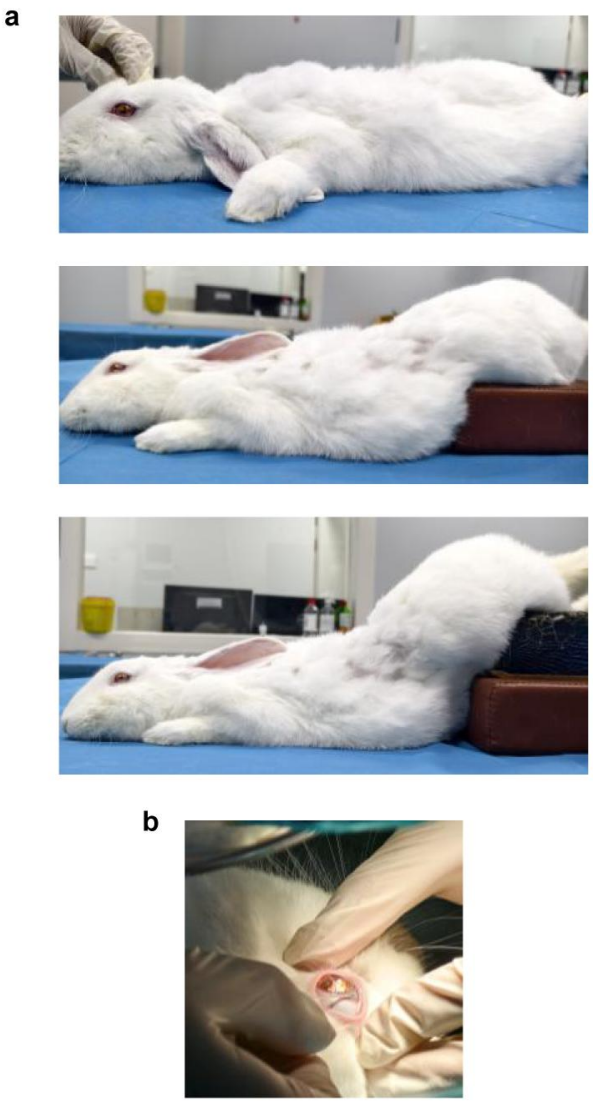

Supplementary Fig. 19: Experimental photographs of rabbit posture manipulation and anterior chamber saline perfusion for inducing corneal-curvature variations.

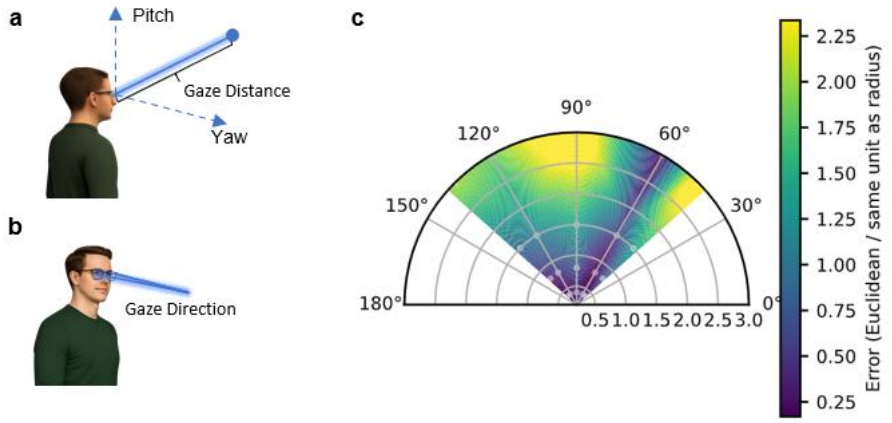

Supplementary Fig. 20: Definition of 3D point of regard and geometric sensitivity without explicit fixation distance. **(a)** Conceptual illustration of three-dimensional point-of-regard (3D PoR) estimation in this work. The 3D PoR is determined by the gaze direction, represented by horizontal (yaw) and vertical (pitch) components, together with the fixation distance along the gaze direction. **(b)** Conceptual illustration of 3D PoR estimation based on binocular gaze intersection. In this approach, gaze directions of the left and right eyes are measured using two RLC-resonant contact lenses mounted on a robotic binocular eye system, and the 3D PoR is obtained from their intersection. **(c)** Geometric sensitivity of conventional binocular-intersection-based 3D PoR reconstruction. As fixation distance increases and the effective angular constraint decreases, small uncertainties in gaze direction lead to rapidly amplified spatial errors.

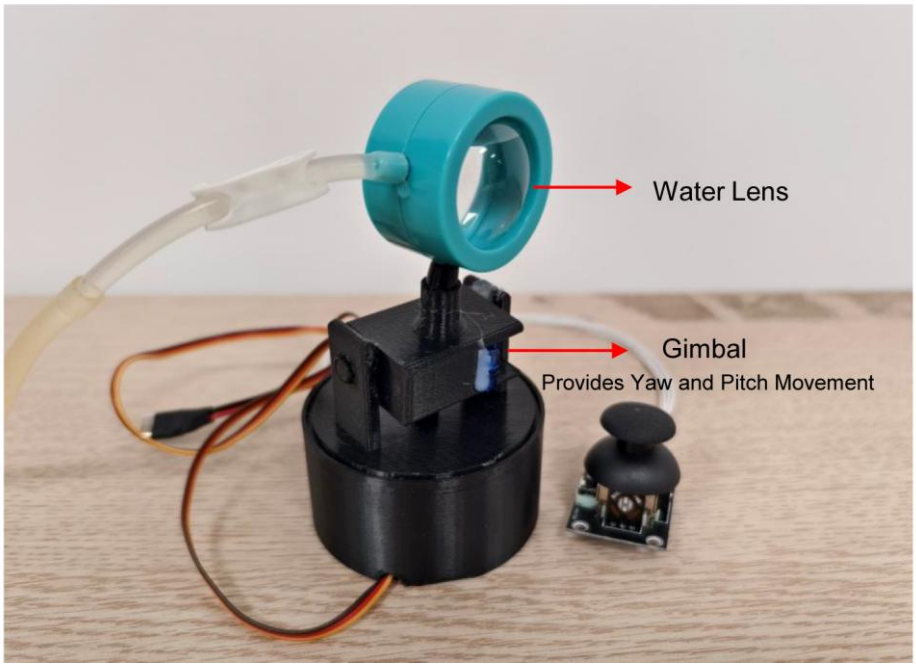

Supplementary Fig. 21: **Water lens and rotation device for simulating joint changes in corneal curvature and gaze direction.**

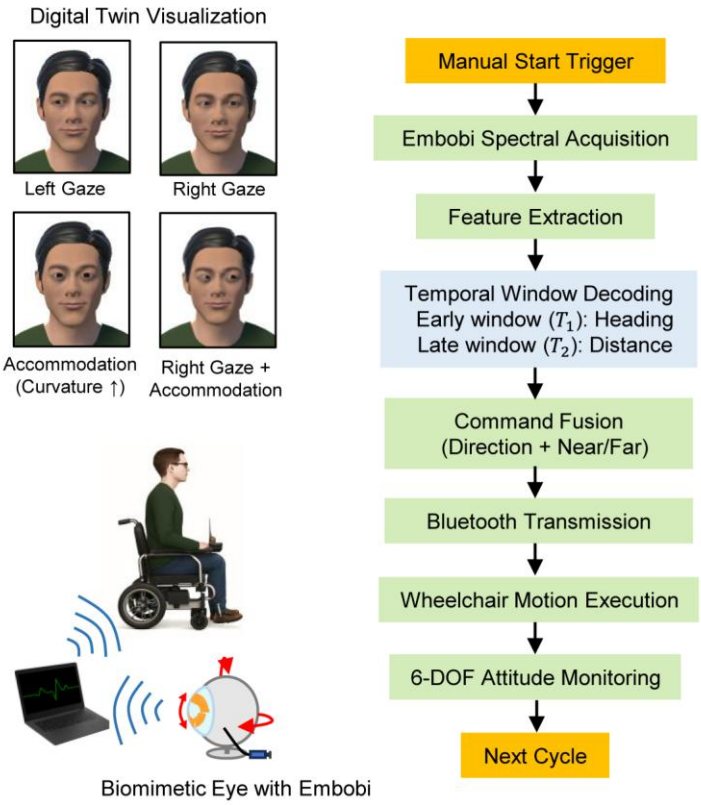

Supplementary Fig. 22: **Target-driven navigation architecture based on embodied 3D fixation.**

	Turns	Width (μm)	Gap (μm)	Inner Diameter (mm)	Outer Diameter (mm)
Coil 1	7	200	100	3.2	7.3
Coil 2	7	160	80	2.56	5.84
Coil 3	9	160	80	2.08	5.84

Supplementary Table.2: Dimensional parameters of the three inductive coils in Embobi.

References

1. Masud, M. *et al.* Measurement Techniques and Challenges of Wireless LC Resonant Sensors: A Review. *IEEE Access* **11**, 95235–95252 (2023).
2. Pierścionek, B. K., Popiolek-Masajada, A. & Kasprzak, H. Corneal shape change during accommodation. *Eye* **15**, 766–769 (2001).
3. Popiolek-Masajada, A., Pierscionek, B. K. & Kasprzak, H. T. Cornea shape and accommodation. in (eds Perina, Sr., J., Hrabovsky, M. & Krepelka, J.) 364–366 (Velke Losiny, Czech Republic, 2001). doi:10.1117/12.417855.
4. Yasuda, A., Yamaguchi, T. & Ohkoshi, K. Changes in corneal curvature in accommodation. *Journal of Cataract and Refractive Surgery* **29**, 1297–1301 (2003).
5. Yasuda, A. & Yamaguchi, T. Steepening of corneal curvature with contraction of the ciliary muscle. *Journal of Cataract and Refractive Surgery* **31**, 1177–1181 (2005).
6. He, J. C., Gwiazda, J., Thorn, F., Held, R. & Huang, W. Change in corneal shape and corneal wave-front aberrations with accommodation. *Journal of Vision* **3**, 1 (2003).
7. Wallace, H. B., McKelvie, J., Green, C. R. & Misra, S. L. Corneal Curvature: the Influence of Corneal Accommodation and Biomechanics on Corneal Shape. *Trans. Vis. Sci. Tech.* **8**, 5 (2019).
8. Gulias-Cañizo, R. *et al.* Applications of Infrared Thermography in Ophthalmology. *Life* **13**, 723 (2023).
9. Matteoli, S., Vannetti, F., Sodi, A. & Corvi, A. Infrared thermographic investigation on the ocular surface temperature of normal subjects. *Physiol. Meas.* **41**, 045003 (2020).
10. Tan, J.-H., Ng, E. Y. K., Rajendra Acharya, U. & Chee, C. Infrared thermography on ocular surface temperature: A review. *Infrared Physics & Technology* **52**, 97–108 (2009).
11. Li, X. *et al.* Temperature Self-Compensating Intelligent Wireless Measuring Contact Lens for Quantitative Intraocular Pressure Monitoring. *ACS Appl. Mater. Interfaces* **16**, 22522–22531 (2024).

Legends for Supplementary Videos 1–5:

Supplementary Video.1: Functional demonstration of Embobi for nine-key eye–machine text input. Based on machine-learning-assisted recognition of eye-writing trajectories, a keyboard display interface was developed to highlight the decoded keys and generate candidate words. As the user continuously wrote the digits 4, 6 and 6 with eye movements, the corresponding keys were successively identified, and the word good was displayed as the predicted text output.

Supplementary Video.2: Demonstration of Embobi-enabled directional eye control in a virtual-reality scene under dark conditions. Gaze-direction commands are used to switch the robotic viewpoint and guide walking navigation, highlighting robust interaction without reliance on ambient illumination.

Supplementary Video.3: In vivo tracking of rabbit eye movements using Embobi. The video demonstrates real-time monitoring of ocular motion in a live rabbit eye with Embobi, illustrating its capability for tracking dynamic eye-movement trajectories in vivo.

Supplementary Video 4: Side-by-side comparison of Embobi and a commercial eye tracker for target discrimination in the same scene, where candidate objects are positioned at similar viewing angles but different depths. Whereas the commercial eye tracker provides ambiguous target assignment under these conditions, Embobi enables reliable target selection by combining fixation-depth decoding with gaze direction. This comparison highlights the limitation of conventional 2D gaze projection when targets are separated primarily in depth. Image appearance differs between the two parts because the commercial eye tracker was recorded using its built-in camera view.

Supplementary Video 5: Representative demonstration of Embobi-guided wheelchair navigation. Extracted from a longer route-execution sequence, this clip shows one target-selection step and the corresponding wheelchair movement toward the fixated spatial location.